A Short-Range FMCW Radar-based Approach for Multi-Target Human-Vehicle Detection

Emanuele Tavanti, *Member, IEEE*, Ali Rizik, *Student Member, IEEE*, Alessandro Fedeli, *Member, IEEE*, Daniele D. Caviglia, *Life Member, IEEE*, and Andrea Randazzo, *Senior Member, IEEE*

***Abstract*—In the present paper, a new microwave-radar-based technique for short-range detection and classification of multiple human and vehicle targets crossing a monitored area is proposed. This approach, which can find applications in both security and infrastructure surveillance, relies upon the processing of the scattered-field data acquired by low-cost off-the-shelf components, i.e., a 24 GHz Frequency Modulated Continuous Wave radar module and a Raspberry Pi mini-PC. The developed method is based on an ad-hoc processing chain to accomplish the automatic target recognition task, which consists of blocks performing clutter and leakage removal with an IIR filter, clustering with a DBSCAN approach, tracking using a Benedict-Bordner α-β filter, features extraction, and finally classification of targets by means of a *k*-Nearest Neighbor algorithm. The approach is validated in real experimental scenarios, showing its capabilities in correctly detecting multiple targets belonging to different classes (i.e., pedestrians, cars, motorcycles, and trucks).**

***Index Terms*—Frequency Modulated Continuous Wave (FMCW) radar data processing, radar imaging, electromagnetic scattering, machine learning.**

I. Introduction

In recent years there has been a growing interest in the development of reliable monitoring and surveillance devices, to be used in urban areas and near critical zones [1]–[4]. A significant push to the development of new systems is also given by the advancements in several applicative scenarios, such as subsurface prospection [5]–[7], non-destructive testing [8], [9], and transportation infrastructure monitoring [10]–[12]. In this framework, short-range radars [13], [14] are particularly interesting because of their robustness against adverse weather conditions and non-sensitivity to lighting conditions [15], [16], problems that can severely affect video-based devices [17]. In particular, the Frequency Modulated Continuous Wave (FMCW) radar technology has been widely adopted in the production of cost-effective and compact systems for several applications [18]–[28]. On the one hand, these radars do not suffer from the severe blind range issues that normally affect monostatic pulsed radars [29]. On the other hand, they are generally cheaper and can cover bigger areas than Light Detection and Ranging (LIDAR) and Long-Wave Infrared (LWIR) devices [16].

On this background, several solutions have been developed [10], [15], [16], [30]–[45]. Often, the proposed approaches involve the use of Machine Learning methods (ML) [46], such as Support Vector Machines (SVM) or Deep Learning Neural Network (DLNN). However, the adoption of DLNNs usually rises issues because of the big amount of training samples that are needed [41]. Works based on Synthetic Aperture Radar (SAR) techniques [47] have been reported, too [10], [42]. Alternative methods for the classification of ground targets are based on the micro-Doppler signatures [44], [48]. Nevertheless, the extraction of a micro-Doppler signature usually requires a quite long illumination of the targets, with consequent practical issues in the presence of relatively fast targets like cars and motorcycles [40]. Despite the great advances in these fields, radar-based ground surveillance with Automatic Target Recognition (ATR) capability for single or simultaneous multiple targets still represents a quite challenging problem. Indeed, many of the methods reported in literature allow the presence of only a single target at a time in the monitored area and systems able to manage multiple targets simultaneously are usually limited to the estimation of the positions and velocities, without ATR capabilities. Finally, compact and low-cost systems are usually required, leading to further limitations in terms of computational resources and achievable radar resolutions. Consequently, there is the need of novel detection techniques, specifically tailored to low-end devices.

In this framework, the present paper presents a new short-range surveillance technique based on low-cost FMCW radar technology, aimed at overcoming the significant limitations in terms of resolution, acquisition speed and ambiguity that afflict this hardware platform. In particular, a novel ad-hoc processing chain able to perform the detection and classification of multiple non-cooperative targets in a cluttered environment has been specifically developed. Firstly, the stretch-processed radar frames are fed into a clutter and leakage removal IIR filter [30], which has been endowed with step-initialization [49] to enhance its transient response and remove potential ringing artifacts. This approach allows to obtain cleaner range-Doppler maps, improving the post-processing performance with respect to the simpler and commonly used background subtraction or single delay-line filter [50]. To isolate the contributions of each target on these maps, the Density-Based Spatial Clustering of

Manuscript received February 22, 2021; revised June 16, 2021; revised October 21, 2021; accepted December 13, 2021. This work was partially supported by Regione Liguria through the POR-FESR project "GenovaSicura" under grant no. G33D0180000D90007.

D. D. Caviglia, A. Fedeli, A. Randazzo, A. Rizik, and E. Tavanti are with the Department of Electrical, Electronic, Telecommunications Engineering and Naval Architecture (DITEN), University of Genoa, 16145 Genoa, Italy (e-mail: {daniele.caviglia, alessandro.fedeli, andrea.randazzo}@unige.it, {ali.rizik, emanuele.tavanti}@edu.unige.it).

Applications with Noise (DBSCAN) method [51] is employed, which assigns a numerical tag to each detected cluster. However, the narrow Doppler unambiguous interval achievable by the employed low-cost radar module could cause clouds of points that lie across the Doppler unambiguous range limits to split, leading to erroneous clustering. To address such an issue, a novel geometrical transformation of the range-Doppler maps has been introduced, with the aim of wrapping such images along the Doppler axis to build the lateral surface of a cylinder. In this way, clusters eventually split are rejoined. This approach also allows to use the original core of the DBSCAN algorithm, without the need of further modifications. In this way, more expensive radar boards with extended Doppler unambiguous range are not needed. Since the DBSCAN is not designed to maintain a coherent association between the cluster tags among the various data frames sequentially acquired by the radar, the detected clusters are tracked using a Benedict-Bordner α-β filter [52] and a proper tracking scheme [13], [29], [53]. Since the tracking needs to be performed on the cylindrically wrapped maps, a set of ad-hoc nonlinear constraints on the state variables has been introduced to force the cluster centroids to remain on the surface of the cylinder. It is also worth highlighting that since the state space in which the tracker works is built upon the wrapped range-Doppler maps, the tracked variables are not anymore in the physical position-velocity space. However, since the only aim is to keep a coherent association of the cluster tags among the range-Doppler maps, this does not affect the recognition of the target types. From the tracked clusters, a set of ad-hoc statistical features related to the Doppler signatures and reflectivity of the targets are extracted, without resorting to micro-Doppler analysis. In particular, differently from other classification schemes, directional statistics estimators [54] are used to compute the features along the aliased Doppler axis. Indeed, these tools fit with the circular nature of the Doppler data more naturally than the classical statistical estimators. Moreover, the reflectivity-related feature is computed by using the whole tracked cluster assigned to a target on the range-Doppler map, instead of considering only the peak amplitude that appears in the range profile as usually done [32], [39]. Indeed, when working on the range spectrum only, the different contributions from simultaneous multiple targets may overlap in the range profile, leading to an unreliable estimation of the reflectivity. In contrast, the clusters on the range-Doppler maps make possible to exploit the differences along both the range and Doppler dimensions, and so reduce the chances of mixing reflections from different targets. Multiple reflections by extended targets are however not taken into account. Finally, the features used for classification are based on the average and variance of the reflectivity through all the frames. Consequently, fluctuations deriving from translational and rotational motion of the targets are implicitly considered and embedded in the data. The classification among four classes (pedestrian, car, motorcycle, and truck) is provided by a properly tuned k-Nearest Neighbor (k-NN) algorithm [46] on the base of a relatively small dataset, not appropriate for adopting deep learning algorithms.

The effectiveness of the approach has been assessed by using a prototype of measurement system realized with only off-the-shelf components, to allow a reduction in the development cost and a faster reproducibility of the proposed setup. In particular, a Distance2Go radar module from Infineon [55], already equipped with transmitting (TX) and receiving (RX) patch antennas, provides the illumination of the monitored area and digitizes the electromagnetic echo returning from the targets, whereas a Raspberry Pi 3 Model B+ mini-PC collects the measurements gathered by the radar board and executes the processing chain. Since the computations are performed locally on a compact and low-power device, this application fulfills the edge computing paradigm [56].

The paper is organized as follows. A detailed description of the developed algorithm for detection, tracking, and classification of the targets is provided in Section II. Section III reports the experimental validation in real operating scenarios. Finally, conclusions are drawn in Section IV.

II. Processing Algorithm

As previously introduced, the developed approach relies upon the use of a FMCW radar, which produces a sequence of wideband chirp signals to illuminate the monitored area. At the transmitting (TX) antenna input terminals, the burst of N_c up-chirps can be expressed as [42], [57]

$$s_{tx}(t) = A_{tx} \sum_{n_c=0}^{N_c-1} \cos[\psi(t)]\, \Pi\left(\frac{t - \frac{T_c}{2} - n_c T_{PRI}}{T_c}\right) \quad (1)$$

where A_{tx} is the signal amplitude, $\psi(t) = 2\pi(f_0 t_s + 0.5\mu t_s^2)$ is the up-chirp phase, T_c is the duration of the single up-chirp, T_{PRI} is the Pulse Repetition Interval (PRI), $t_s = t - n_c T_{PRI}$ (being $t_s \in [0, T_c]$ known as fast-time and n_c slow-time index), f_0 is the starting frequency, $\mu = B/T_c$ is the sweep rate, B is the bandwidth of the sweep, and $\Pi(\chi)$ evaluates to 1 when $|\chi| \leq 1/2$ and to 0 otherwise. Between a pair of adjacent up-chirps, a recovery time is usually placed (i.e., $T_{PRI} > T_c$), during which the frequency synthesizer returns to the initial condition and the relative echo signal is neglected. The burst of chirps, known also as frame, lasts $T_{CPI} = T_{PRI} N_c$, where CPI stands for Coherent Processing Interval. A proper interval is generally interposed to the next burst; the frame period T_f is then longer than T_{CPI}. Fig. 1 exemplifies the structure of the signal.

The backscattered wave, which is a delayed and attenuated copy of the transmitted one, is captured by a dedicated RX antenna and demodulated by an I/Q mixer returning an

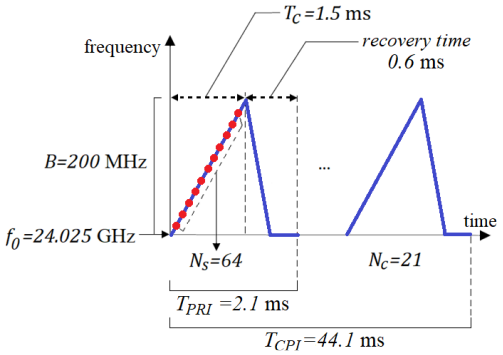

Fig. 1. Time-frequency representation of the transmitted signal.

Intermediate Frequency (IF) signal. Thereafter, this signal is sampled by an ADC and collected in a data matrix. Neglecting higher order and constant terms in the IF signal phase and the range-doppler coupling [29], [42], [50], the matrix representing a single data frame can be stated as follows [13]

$$q_{IF}(n_s, n_c) = A_{IF} e^{j2\pi(f_b T_s n_s - f_D n_c T_{PRI})}, \quad n_s = 0, \dots, N_s - 1, \;\; n_c = 0, \dots, N_c - 1 \tag{2}$$

where $A_{IF} \propto A_{rx}$, with A_{rx} strength of the received echo, T_s is the sampling period, $f_D = -2v_r/\lambda_0$ is the Doppler shift, v_r is the radial velocity ($v_r > 0$ for departing targets), $\lambda_0 = c/f_0$ is the wavelength, c being the speed of light, and $f_b = \mu\tau_0$ (known as FMCW radar range equation [58]) is the beat frequency, with $\tau_0 = 2r_0/c$ time-of-flight for the range r_0 at the start of the chirp. The second term in the exponent of (2) is known as spatial Doppler [29]. For simplicity, this analysis assumes that a single point-like target is present. If multiple targets with several reflective points exist (extended targets are usually modeled with different point-like scatterers in this framework), then the mixer output will be the sum of the IF signals related to each point [2], [15], [38], [43]. It is worth remarking that, in principle, a matched filter could also be used to extract the target responses from the measured signal. However, the adopted low-cost FMCW board does not allow a direct access to the received echo, but it only provides samples of the deramped signal in (2). Consequently, a convolution with the matched signal cannot be performed. Instead, a Fourier-based processing scheme has been adopted, as often done in short-range FMCW radars applications.

The target identification method starts when the amplitude of the echo signal crosses a user-defined threshold (i.e., when one or more targets enter the monitored area). Initially, all the radar frames are collected until the event ends (i.e., the amplitude of the echo falls below the threshold). Each recorded frame passes through a clutter and leakage removal filter (detailed in Section II.A) before the check of the threshold crossing. Moreover, care is taken to discard events caused by scintillation in the echo signal and to avoid the premature stop of the recording when moving targets are still present [29], [53]. After all the frames are collected, they are processed by using the chain shown in Fig. 2. Details about the various blocks are provided below.

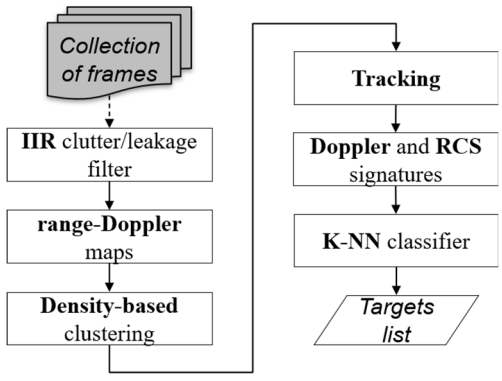

Fig. 2. Processing chain for the surveillance radar device prototype.

A. Clutter and leakage removal

A Moving Target Indication (MTI) filtering technique [53] is firstly applied to cope with the RX-TX leakage [13] and the clutter caused by static objects [50]. In particular, an IIR filter [30] is employed in this work. The filtered frame can be expressed as follows

$$u(n_s, n_c) = q_{IF}(n_s, n_c) - q_{IF}(n_s, n_c - 1) + K_c u(n_s, n_c - 1) \tag{3}$$

where K_c is a user-defined parameter ($0 \le K_c < 1$ to guarantee stability). It is interesting to highlight that for $K_c = 0$ the filter reduces to a standard single delay-line canceller [53]. It is worth noting that, in short-range radar system for monitoring applications, the issues related to the transient response of IIR filters are often neglected [30]. Indeed, from (3) it can be seen that $u(n_s, 0) = q_{IF}(n_s, 0)$, i.e. the first demodulated chirp is not filtered and, entering the feedback of the filter, can negatively affect the transient response, inducing ringing effects on the range-Doppler maps [50], [53]. To mitigate this drawback, a step initialization technique [49] is used. Specifically, the state variable of the filter is initialized to $(1 - K_c)^{-1} q_{IF}(n_s, 0)$, so that the output at $n_c = 0$ is forced to zero and thus ringing is dumped. Due to this correction, the first filtered chirp of a frame is always a null vector, so it can be discarded, leading to an effective coherent processing interval $T_{CPI,eff} = T_{PRI}(N_c - 1)$.

B. Computation of the Range-Doppler maps

After clutter and leakage removal has been performed, the range-Doppler maps are obtained as follows

$$M^{(K_c, K_{sf})}(q_{IF})(\hat{n}_b, \hat{n}_D) = \mathcal{D}_D^{(N_D)} \left[\mathcal{D}_r^{(N_R)} \left(u^{(K_c)} w_r^{(K_{sf})} \right) w_D^{(K_{sf})} \right] (\hat{n}_b, \hat{n}_D) \tag{4}$$

where $u^{(K_c)}$ is the filtered frame computed as in (3) with filter parameter K_c, $w_r^{(K_{sf})}$ and $w_D^{(K_{sf})}$ are Kaiser windows with shape factor K_{sf} to be applied on the beat frequency and Doppler dimensions, respectively, whereas $\mathcal{D}_r^{(N_R)}$ and $\mathcal{D}_D^{(N_D)}$ are the range-FFT and Doppler-FFT operators with preliminary zero-padding to achieve sequences of length N_R and N_D, respectively (N_R and N_D should be powers of two for optimal performance of the FFTs). The resulting spectrum along the beat frequency dimension has support $(-1/2T_s, 1/2T_s]$, but, because of (2), only the interval $[0, 1/2T_s]$ is retained (its bins are indexed by $\hat{n}_b$ in the following); this corresponds to the interval $[0, N_s c/4B]$ on the range axis r obtained through the FMCW radar range equation. The spectrum along the Doppler axis has support $(-1/2T_{PRI}, 1/2T_{PRI}]$, and the related bins will be indexed by $\hat{n}_D$; this interval can be rescaled to $(-c/4T_{PRI}f_0, c/4T_{PRI}f_0]$ for the radial velocity v_r through the Doppler shift relation. The windowing and the zero-padding are used to mitigate sidelobes [29], [52] and to obtain better interpolated maps [13], [47], respectively. It is worth remarking that when targets are present in the illuminated scene, clouds of points having high amplitude appear in the range-Doppler maps; custom features can be extracted from them and used to identify the target type, as discussed in the following.

C. Density-based clustering

When dealing with not point-like targets, they appear on the range-Doppler map as clouds of points. Therefore, it is necessary to apply a clustering method to associate these groups of points to the underlying real objects and so computing the

features to classify them coherently. The chosen method is the DBSCAN [51], which assigns a numerical tag to each detected cluster. This algorithm is particularly interesting because it does not require the knowledge of the number of clusters to be searched and it is potentially able to identify spurious aggregation of points as noise. This feature, together with the adoption of a tracking scheme, is also useful to remove ghost targets generated by multipath reflections. Indeed, the appearance of multipath reflections on the range-Doppler maps is hardly exploitable for classification, because of their strong dependance on a-priori unknown and barely predictable environmental factors, and they can be expected to act more as a flickering disturbance to be removed.

However, this method cannot be applied directly to the range-Doppler maps. In fact, as indicated in Section III, the radar board adopted in this work has an unambiguous interval along the radial speed (Doppler) axis equal to $(-v_{r,max}, v_{r,max}]$, where $v_{r,max} \cong 5.4\,\mathrm{km/h}$, which is quite limited. Consequently, every target whose Doppler spread extends beyond this interval will be affected by aliasing and it could be split on the range-Doppler map. This would lead the DBSCAN to identify more clusters than the number of actual targets. As an example, Fig. 3(a) shows this phenomenon on a range-Doppler map acquired in presence of a pair of pedestrians.

To mitigate this issue without resorting to more expensive radar modules with extended Doppler unambiguous range, an ad-hoc solution is introduced. The range-Doppler map is wrapped along the Doppler axis to build the lateral surface of a cylinder, and this is embedded in a 3D Euclidean space. In this way, the spectrum eventually split at the Doppler unambiguous limits is rejoined. First, the indexes $\hat{n}_b$ and $\hat{n}_D$ adopted in (4) for the original range-Doppler map are converted to range and radial velocity as follows

$$r = \hat{n}_b \frac{d_b c}{2\mu}, \quad v_r = \hat{n}_D \frac{d_D c}{2 f_0} \tag{5}$$

where d_b and d_D are the widths of the bins for the beat and Doppler frequencies, respectively. Thereafter, the following transformation of coordinates is introduced

$$\vec{\mathbf{T}}(r, v_r) = \begin{bmatrix} \frac{v_{r,max}}{\pi} \cos\left(\pi \frac{v_r + v_{r,max}}{v_{r,max}}\right) \\ \frac{v_{r,max}}{\pi} \sin\left(\pi \frac{v_r + v_{r,max}}{v_{r,max}}\right) \\ r \end{bmatrix} = \begin{bmatrix} v_r' \\ v_r'' \\ r \end{bmatrix} \tag{6}$$

Such a transformation maps the $[r, v_r]^t$ coordinates of the original range-Doppler map to the variables $[v_r', v_r'', r]^t$ that define Cartesian coordinates restricted to the lateral surface of a cylinder. In particular, r varies along the height of the cylinder (i.e., the unambiguous range interval $[0, N_s c/4B]$), whereas v_r' and v_r'' are transversal coordinates restricted to the circular cross-section. Moreover, the following operator, performing a transformation in the opposite direction, is introduced

$$\overleftarrow{\mathbf{T}}(v_r', v_r'', r) = \begin{bmatrix} \theta \frac{r}{\pi} \frac{v_{r,max}}{\pi} - v_{r,max} \end{bmatrix} = \begin{bmatrix} r \\ v_r \end{bmatrix} \tag{7}$$

where $\theta \in (0, 2\pi]$ is the polar angle corresponding to the point $[v_r', v_r'']^t$. Finally, the wrapped range-Doppler map can be formally stated as

$$\widehat{M}^{(K_c, K_{sf})}(q_{IF})(v_r', v_r'', r) = M^{(K_c, K_{sf})}(q_{IF}) \left\{ \left[\frac{2\mu}{d_b c}, \frac{2 f_0}{d_D c} \right]^t \odot \overleftarrow{\mathbf{T}}(v_r', v_r'', r) \right\} \tag{8}$$

where $\odot$ is the entry-wise product. Fig. 3(b) exemplifies this result starting from the split spectrum of Fig. 3(a).

The DBSCAN is then fed with each single wrapped range-Doppler map (8). By adopting this transformation and by endowing the DBSCAN algorithm with the canonical 3D Euclidean metric to measure the distance between points on the wrapped range-Doppler maps, it is possible to keep the original core of the method without further modifications. Only the points in which the maps have an amplitude equal or higher than the user-defined parameter th_{RD} are considered for the clustering and the following processing blocks. Further parameters of the DBSCAN method are the radius ϵ of a sphere centered at a given point in which its neighbors are searched for, and the minimum number of points M that must be present in this sphere in order not to identify the central point as noise.

The DBSCAN returns a tag for each point present in the thresholded and wrapped map, allowing the detection of N_{clu} clusters; for each one, a centroid on the cylindrical surface is computed, whose coordinates are $\left[v_{r,l}', v_{r,l}'', r_l\right]^t$, $l = 1, \ldots, N_{clu}$.

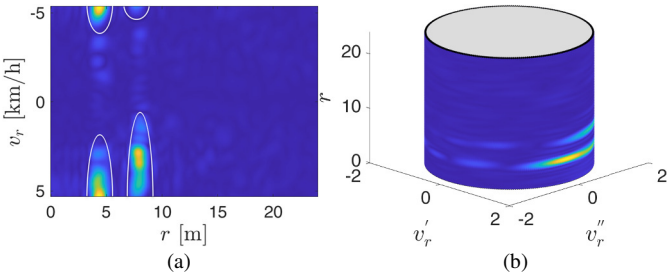

Fig. 3. (a) Range-Doppler map in the presence of a pair of pedestrians (the white curves indicate the portions of the split Doppler spread). (b) Map in (a) wrapped along the Doppler axis.

D. Benedict-Bordner smoothing

The DBSCAN method cannot guarantee that the same cluster tag is assigned to the same underlying real target among consecutive range-Doppler maps. Therefore, it is necessary to apply a tracking method that allows maintaining the correct associations between them. In particular, the motion of the centroids of the clusters on the wrapped range-Doppler maps will be tracked. It is important to point out that a direct and accurate tracking of the target positions and velocities is not needed, since the final aim of the tracking is to just maintain the association between clusters and real targets among subsequent frames. The temporal sequence of associations between tags and centroids, together with the history of the related state vector (defined below), is referred to as a track, whose temporal extension corresponds to the presence of a target in the scene. It is worth noting that, as previously discussed, the narrow Doppler unambiguous range provided by the adopted low-end radar board may produce clusters split on the range-Doppler maps, thus not allowing an effective tracking. Consequently, the tracking algorithm has been modified to work on the wrapped maps defined in the previous section.

As it can be seen in (6), in this case the dynamics of the centroids are non-linear, since they are constrained to move on the lateral surface of a cylinder. However, the adoption of an approximated linear model, if properly parameterized and constrained [59], has been proven experimentally to achieve the needed performance, as will be shown in Section III. Moreover, this leads to a lower computational burden with respect to tracking methods designed to deal with non-linear models (e.g., Extended Kalman Filter [59]). Based on these considerations, the dynamical model chosen was the DWNA (Discrete White Noise Acceleration) [60], which can be written as

$$\begin{aligned}\mathbf{s}(n+1) &= \mathbf{A}\mathbf{s}(n) + \mathbf{B}a(n)\\ \mathbf{m}(n) &= \mathbf{C}\mathbf{s}(n)\end{aligned} \tag{9}$$

where n is the time index of the frame (corresponding to a wrapped range-Doppler map), $\mathbf{m}(n) = [v_r'(n), v_r''(n), r(n)]^t$ is the measurement vector containing the position of the considered centroid (the index l of the corresponding cluster is dropped to simplify the notation), a is an acceleration modelled as white noise with zero mean value, $\mathbf{s}(n) = \left[v_r'(n), u_{v_r'}(n), v_r''(n), u_{v_r''}(n), r(n), u_r(n)\right]^t$ is the state vector, $\mathbf{B} = [T^2/2, T, T^2/2, T, T^2/2, T]^t$ (a normalized time step can be considered here, i.e. $T = 1$), and

$$\mathbf{A} = \mathrm{diag}\begin{pmatrix}1 & T\\ 0 & 1\end{pmatrix}, \mathbf{C} = \begin{bmatrix}1 & 0 & 0 & 0 & 0 & 0\\ 0 & 0 & 1 & 0 & 0 & 0\\ 0 & 0 & 0 & 0 & 1 & 0\end{bmatrix} \tag{10}$$

To tackle with the non-linear motions of the clusters on the wrapped maps, it is also required that the centroid of a cluster, i.e., $[v_r'(n), v_r''(n), r(n)]^t$, strictly remains on the cylinder and, consequently, its velocity vector, i.e., $\left[u_{v_r'}(n), u_{v_r''}(n), u_r(n)\right]^t$ is tangent to the lateral surface of the cylinder. Therefore, a set of ad-hoc constraints have been added, i.e.,

$$\begin{bmatrix}v_r'(n)\\ v_r''(n)\\ r(n)\end{bmatrix} \in S, \begin{bmatrix}u_{v_r'}(n)\\ u_{v_r''}(n)\\ u_r(n)\end{bmatrix} \in \mathcal{T}(S), \forall n \tag{11}$$

where S is the surface generated by wrapping the range-Doppler map and $\mathcal{T}(S)$ is the tangent space to this surface.

Now that the dynamical model has been introduced, it is necessary to choose an appropriate smoothing filter. One of the most popular ones is the Kalman filter [59], but it has the disadvantage of requiring the knowledge of the noise that affects the system. Therefore, since the noise can vary even between different installation environments, an α-β filter, which does not require such information, was adopted [52]. In particular, differently from commonly-adopted approaches, the Benedict-Bordner version [52] of the α-β filter has been used. In this way, only the parameter α needs to be defined, being $\beta = \alpha^2/(2-\alpha)$, whereas the original α-β filter requires both α and β to be heuristically selected. The adopted filter is based on the following predictor-corrector scheme:

- Prediction: the state in n is estimated by propagation of the corrected estimated state in $n-1$ as

$$\begin{aligned}\hat{\mathbf{s}}(n|n-1) &= \mathcal{N}[\mathbf{A}\hat{\mathbf{s}}(n-1|n-1)]\\ \hat{\mathbf{m}}(n|n-1) &= \mathbf{C}\hat{\mathbf{s}}(n|n-1)\end{aligned} \tag{12}$$

  where $\hat{\mathbf{s}}(n|n-1)$ and $\hat{\mathbf{m}}(n|n-1)$ are the estimated state and measurements in n, respectively, predicted on the base of the measurements available until $n-1$, whereas $\hat{\mathbf{s}}(n-1|n-1)$ is the corrected estimated state on the base on the measurements available until $n-1$. The operator $\mathcal{N}(\cdot)$ projects the state to enforce (11) [59].
- Correction: the estimated state achieved in the prediction stage is corrected on the base of $\mathbf{m}(n)$ as follows

$$\begin{aligned}&\hat{\mathbf{s}}(n|n) =\\ &\mathcal{N}\{\hat{\mathbf{s}}(n|n-1) + \boldsymbol{\mathcal{G}}[\mathbf{m}(n) - \hat{\mathbf{m}}(n|n-1)]\}\end{aligned} \tag{13}$$

  where $\boldsymbol{\mathcal{G}}$ is a 6×3 matrix with value α in the positions $(1,1), (3,2), (5,3)$, value β in the positions $(2,1), (4,2), (6,3)$, and zero elsewhere.

Finally, the operator $\mathcal{N}$ that enforce the constraints in (11) is formulated as

$$\mathcal{N}\left\{\begin{bmatrix}v_r'\\ u_{v_r'}\\ v_r''\\ u_{v_r''}\\ r\\ u_r\end{bmatrix}\right\} = \begin{bmatrix}\frac{v_{max}}{\pi}\cos\breve{\theta}\\ u_{v_r'} - \left[u_{v_r'}\cos\breve{\theta} + u_{v_r''}\sin\breve{\theta}\right]\cos\breve{\theta}\\ \frac{v_{max}}{\pi}\sin\breve{\theta}\\ u_{v_r''} - \left[u_{v_r'}\cos\breve{\theta} + u_{v_r''}\sin\breve{\theta}\right]\sin\breve{\theta}\\ r\\ u_r\end{bmatrix} \tag{14}$$

where $\breve{\theta}$ is the polar angle identified by the unconstrained v_r' and v_r'' coordinates. Specifically, the operator $\mathcal{N}$ projects the unconstrained point $[v_r', v_r'', r]^t$ on the surface of the cylinder having radius v_{max}/π, i.e., on the wrapped range-Doppler map. Moreover, the operator $\mathcal{N}$ removes the normal component from the unconstrained vector $\mathbf{v} = \left[u_{v_r'}, u_{v_r''}, u_r\right]^t$ by subtracting the quantity $(\mathbf{v}\cdot\mathbf{n}_{\breve{\theta}})\mathbf{n}_{\breve{\theta}}$, where $\mathbf{n}_{\breve{\theta}} = \left[\cos\breve{\theta}, \sin\breve{\theta}, 0\right]$ is the radial unit vector of the considered cylindrical coordinate system.

E. Tracking scheme

Beyond the state estimates, it is important to discover and delete tracks corresponding to false targets (namely, corresponding to spurious signals, such as the ones generated by multipath reflections), to follow flickering targets, and to understand when a new target enters the monitored area or an old one leaves it [13], [29], [53]. To this end, different schemes has been considered in the literature. Several advanced tracking schemes employing probabilistic models of association have also been recently proposed [29], [53]. However, such approaches require the a-priori knowledge of some probability distributions, e.g., those related to the errors of measure, which may be quite challenging to be determined since they can vary between different installations. Consequently, in the proposed approach a non-parametric method (which does not require the a-priori knowledge of any probability distributions) has been used for the association between detected centroids and tracks.

In particular, the tracking scheme shown in Fig. 4 is used. Each track employs a data structure storing the history of the associations between the cluster tags and the centroids, among the temporally sorted collection of wrapped range-Doppler maps, and of the state variables smoothed by the Benedict-Bordner filter (presented in the previous Section). Moreover, each track has two properties: age and vis. The former counts the number of past frames from the creation of the track, whereas the latter counts the number of past frames in which the track was associated with a detected cluster centroid.

The steps of the scheme sketched in Fig. 4 can thus be summarized as follows:

1. Creates an empty list of tracks. Initialize the frame counter $Mc = 1$.
2. Take the Mcth wrapped range-Doppler map.
3. Detect the centroids for each cluster in the current wrapped range-Doppler map.
4. If the list of tracks is empty (e.g., it happens when $Mc = 1$) then jump to the step 8.
5. Assign the detected centroids to pre-existing tracks by means of a cost matrix [53], where each row corresponds to a pre-existing track, and each column is related to a detected centroid. This matrix is compiled associating to each track-centroid pair a cost given by the value of the Euclidean distance between the estimated position of the track (equation (12)) and the detected centroid. A parameter R_{gate}, which defines a limit for a detected centroid to be associated with a track, is also introduced. In particular, if the distance between the centroid previously assigned to the track and the actual one is higher than R_{gate}, then the cost is set $+\infty$, preventing the association. Once the matrix is compiled, the assignment is performed as follows
   a. Select the ijth element of the matrix with minimum cost.
   b. Assign the pre-existing track i to the detected centroid j.
   c. Substitute all the costs in the row i and the column j with $+\infty$.
   d. If there are no more finite costs in the matrix, then return the lists of the associations and of not assigned centroids and tracks. Otherwise, jump to step a.
6. Update the tracks. In particular, for each track associated to a new centroid, correct its state with the detected centroid through (13), and increase the age and vis counters of these tracks, i.e. $age \rightarrow age + 1$ and $vis \rightarrow vis + 1$. For each track not assigned to a new centroid, increase only its age counter.
7. If a track is not associated to a centroid for N_u consecutive frames, then consider its underlying target as departed from the monitored area and fill its related row in the next cost matrices with $+\infty$ (in this way it will not be assigned to future detections). Delete the tracks for which $vis/age < th_v$, where th_v is a user-defined parameter. This operation attempts to discard false tracks associated to scintillation in the echo signal or multi-bounce reflections.
8. For each centroid not associated with a pre-existing track, create a new track, initialize with the measured $\mathbf{m} = [v_r', v_r'', r]^t$ the track state vector as $\mathbf{s} = [v_r', 0, v_r'', 0, r, 0]^t$, create a new instance of the Benedict-Bordner filter for it, and finally set the age and vis counters to zero.
9. If other range-Doppler maps remain to be processed, then set $Mc \rightarrow Mc + 1$ and jump to step 2. Otherwise, delete the tracks that have been visible for less than 3 frames. This operation aims to delete the false tracks that could be instantiated when the last target in the scene exits passing very near to the radar, generating many spurious reflections.

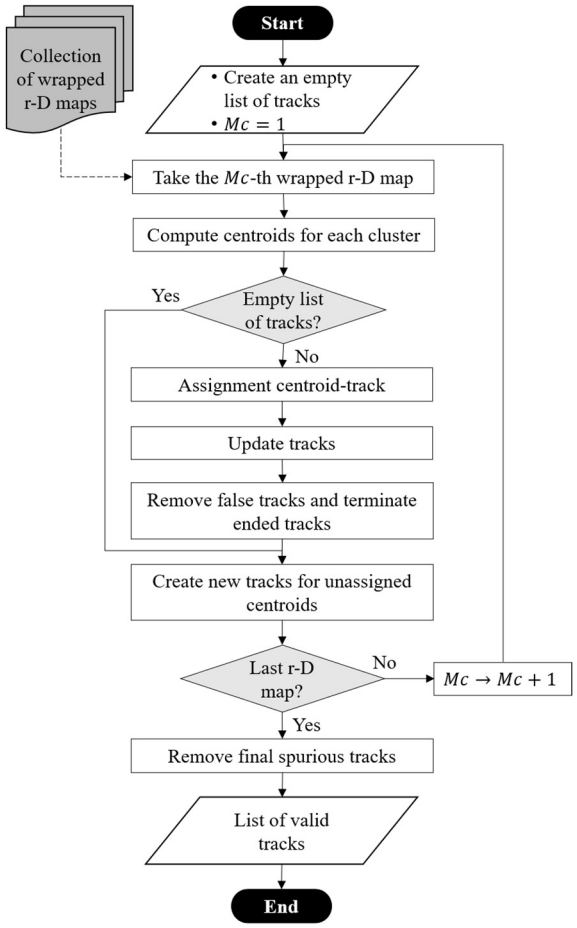

Fig. 4. Tracking scheme.

It is worth noting that the MTI filter deletes the contributions given by any static object. However, if a target enters the scenario and stops during the crossing, the tracking algorithm is still able to keep its track, provided that the number of frames in which the target does not move is sufficiently low (i.e., if $vis/age \geq th_v$). If the number of frames in which the target is stopped is high (i.e., when $vis/age < th_v$), the related track is discarded. Consequently, when the target restarts a new track is initialized. Such a situation can be mitigated by increasing the parameter th_v, so preventing a premature deletion of a track.

Finally, it should be noted that the developed approach processes the echoes collected during the whole passage of the targets through the monitored area. Consequently, if one target is shadowed for some frames, the tracking method tries to estimate its movements on the wrapped range-Doppler map to not confuse its track with the ones belonging to other targets present in the monitored area. In this way, it is still possible to classify a target that was temporarily shadowed during its passage.

F. Doppler and RCS signature extraction

In this Subsection, the features used to characterize the targets for classification are outlined. At first, propaedeutic quantities regarding the reflectivity and the Doppler signature

of the targets are introduced. Thereafter, the composition of the feature vector for the classification is presented.

1) Target reflectivity

The target reflectivity can be expected to vary significantly among pedestrians, motorcycles, cars, and trucks [32], [39], hence it can be useful for classification. This information is provided by the Radar Cross Section (RCS) [39], [53], [61], which can be expressed using the radar equation as

$$\sigma = K_A r^4 \frac{P_{rx}}{P_{tx}} \tag{15}$$

where $K_A = (4\pi)^2/(GA_e)$ [m^{-2}] is a system constant (with G and A_e gain and effective area of the antennas, respectively), r is the target range in the far-field region, whereas P_{tx} and P_{rx} are the transmitted and received power, respectively.

It is worth noting that, for classification purposes, an accurate estimation of the actual target RCS is not necessary, but it is sufficient to have an indicator related to such a parameter. In this view, noting that P_{rx}/P_{tx} is proportional to $|A_{rx}|^2/|A_{tx}|^2$, the following quantity, which is related to the square root of σ/K_A, may be adopted for classification purposes [39]

$$\gamma = r^2 \frac{|A_{rx}|}{|A_{tx}|} \tag{16}$$

Since $A_{IF} \propto |A_{rx}|$, γ is usually directly estimated from the peak amplitude that appears in the range profile (given by a single range-FFT applied on the IF signal) [39]. However, this approach assumes the presence of a single target at a time. Indeed, when multiple targets are simultaneously present in the monitored area, their contributions may overlap in the range profile, leading to an unreliable estimation. Moreover, extended targets (e.g., trucks) are usually characterized by several dominating reflecting points, which may appear separated both in the range and Doppler dimensions. This information, which can strengthen the classification, is lost when considering only the major peak in the range-FFT.

To overcome such issues, in this work a new RCS-related feature is defined starting directly from the range-Doppler map instead of using the single range profile. In particular, the following RCS-related quantity is used

$$\tilde{\gamma}_{i,j} = \sum_{\hat{n}_D,l}^{P_{i,j}^D, P_{i,j}^R(\hat{n}_D)} \left[\frac{r_l^{1.8}}{N_s} \left| M^{(K_c,K_{sf})}\left(q_{IF,j}\right)\left(\hat{n}_{b,l}, \hat{n}_D\right) \frac{\sqrt{f_c^2 + f_{b,l}^2}}{f_{b,l}} \right| \right]^2 \tag{17}$$

where $P_{i,j}^D$ is the set of Doppler bins contained in the cluster belonging to the ith tracked target at the jth frame, $P_{i,j}^R(\hat{n}_D)$ is the set of range bins in which local peaks detected along the $\hat{n}_D$th range profile occur (this range profile is delimited by the cluster limits), whereas r_l, $\hat{n}_{b,l}$, and $f_{b,l}$ are the range, the range bin and the beat frequency for the lth peak, respectively. The dependence on $|A_{tx}|$ existing in (16) has been neglected since it is only a system constant. Provided that the targets are separated at least in one dimension (range or Doppler), this indicator can be expected to be less altered by the presence of other targets with respect to the one proposed in [39]. Moreover, it considers the possibility to have several dominating scattering points for an extended target. The exponent of r in (17) has been empirically modified to account for the not free-space propagation, as suggested in [39]. The last multiplying fraction in (17) compensates for the non-flat transfer function of the analog IF amplifier (f_c is the lower corner frequency) that is usually placed before the ADC. The dividing coefficient N_s and the square inside the sum have been empirically inserted to better scale the values on the base of the results achieved by a preliminary test with the learning method discussed in the following.

It is worth remarking that the reflectivity may be affected by the characteristics of the targets, especially for pedestrians. Specifically, in [62] an average reduction of 5 dBsm has been observed between a child and an adult in the range 23-28 GHz and considering the full range of the azimuthal angle. However, in our settings, the class of adult pedestrians is the one already showing the lower RCS, and, consequently, it is expected that children, having lower values, would be still classified as pedestrians. Moreover, the variability caused by different clothes is quite low and is expected to have a negligible impact: for an adult it has been found to be less than ± 1 dBsm, especially when clothes are electrically thin and dry [62], [63]. Finally, concerning the posture, although the different poses during walk may introduce fluctuations in the RCS [63], such a behavior is implicitly taken into account in building the feature vector. Indeed, as detailed in Section II.F.3, all the frames (for which the pedestrians assume different poses) are considered.

2) Doppler signature

The Doppler signature has been widely adopted for ATR tasks [37], [38], [40], [64]–[66]. This parameter depends upon the radial velocities of the target scattering points. In particular, in this work, the spread that a target presents along the Doppler dimension is considered [38]. This spread is here estimated by computing the variance of the Doppler spectrum associated with a tracked cluster. Because of the already discussed aliasing phenomenon, the wrapped range-Doppler maps are considered again, and, because of the circular structure of this data, the variance is here computed by means of directional statistics [54]. In particular, the following estimator is used

$$S_{i,j} = 1 - \overline{R}_{i,j} \tag{18}$$

where $S_{i,j}$ is the circular variance computed for the ith tracked cluster at the jth frame, $\overline{R}_{i,j} = \left|\zeta_{i,j}\right|/N_{i,j}^{\theta}$ with $\zeta_{i,j} = \sum_{l=1}^{N_{i,j}^{\theta}} e^{j\theta_{i,j}^l}$, and $\theta_{i,j}^l$ are the $N_{i,j}^{\theta}$ angular positions of the cluster points (on the wrapped map).

3) Feature vector

The feature vector for the ith track is then defined as

$$\mathbf{x}_i = \begin{bmatrix} E(S_i) \\ \mathrm{var}(S_i) \\ E(\tilde{\gamma}_i) \\ \mathrm{var}(\tilde{\gamma}_i) \\ E\left(\left|\tilde{v}_{r,i}\right|\right) \end{bmatrix} = \begin{bmatrix} \frac{1}{vis}\sum_{j=1}^{vis} S_{i,j} \\ \frac{1}{vis-1}\sum_{j=1}^{vis}\left[S_{i,j} - E(S_i)\right]^2 \\ \frac{1}{vis}\sum_{j=1}^{vis} \tilde{\gamma}_{i,j} \\ \frac{1}{vis-1}\sum_{j=1}^{vis}\left[\tilde{\gamma}_{i,j} - E(\tilde{\gamma}_i)\right]^2 \\ E\left(\left|\tilde{v}_{r,i}\right|\right) \end{bmatrix} \tag{19}$$

where $E(\cdot)$ is the sample mean, $\mathrm{var}(\cdot)$ is the non-biased sample variance, $\tilde{v}_{r,i}$ is the radial velocity (estimated by considering the range displacement of the centroid between frames), whereas $S_i = \{S_{i,j}\}_{j=1}^{vis}$ and $\tilde{\gamma}_i = \{\tilde{\gamma}_{i,j}\}_{j=1}^{vis}$ are the sets of circular variances (18) and RCS-related estimations (17), respectively, in the frames where the ith target is visible. It is worth noting that the angular dependence of the RCS and the fluctuations due to posture are implicitly considered in building the feature vector. Indeed, the feature vector contains the average and variance of the RCS-related function in (17), which is evaluated for each range-Doppler image gathered during the crossing of the targets in front of the radar. Since the targets usually exhibit both translational and rotational motion, the reflectivity data corresponding to different aspect angles and poses are collected. Moreover, although in some cases there could be a stronger/nearer target overwhelming the direct response of a weaker target (e.g., through secondary lobes), this is expected to last for a limited number of frames, and consequently the feature creation mechanism is expected to compensate it.

As usually done in machine learning, the feature vector $\mathbf{z}_i$ effectively adopted for classification is standardized, namely, the jth feature for the ith vector is obtained as follows

$$z_{i,j} = \frac{x_{i,j} - \overline{x^{(j)}}}{\sqrt{\frac{1}{1-\sum_{l=1}^{N} w_l^2} \sum_{l=1}^{N} w_l \left(x_{l,j} - \overline{x^{(j)}}\right)^2}} \tag{20}$$

where $x_{i,j}$ is the jth feature of $\mathbf{x}_i$ defined in (19), N is the number of available observations, w_l are weights used in presence of unbalanced reference set (with $\sum_{l=1}^{N} w_l = 1$), and $\overline{x^{(j)}} = \sum_{l=1}^{N} w_l x_{l,j}$ is the weighted average of the jth feature among all the reference set.

G. k-NN classification

The chosen classification method is the k-NN [46]. If the standardized reference set $Z = \{\mathbf{z}_l \in \mathbb{R}^5\}_{l=1}^{N}$ and the related labels $Y = \{y_l \in \{1, \dots, C\}\}_{l=1}^{N}$, with C number of classes, are available, the classification of a new standardized feature vector $\hat{\mathbf{z}}$ is done according to the following steps

1. Compute the N distances between the reference set elements and $\hat{\mathbf{z}}$ through a previously selected metric.
2. Select the k elements having the lowest distances. Collect the indexes of these vectors in the set $\mathcal{D}(\hat{\mathbf{z}})$.
3. Assign to $\hat{\mathbf{z}}$ the class that maximizes the following posterior probability

$$p(c|\hat{\mathbf{z}}) = \frac{\sum_{l \in \mathcal{D}(\hat{\mathbf{z}})} w_l I(c, \mathbf{z}_l)}{\sum_{l \in \mathcal{D}(\hat{\mathbf{z}})} w_l} \tag{21}$$

where $I(c, \mathbf{z}_l)$ is a function that returns 1 if $\mathbf{z}_l$ belongs to the class c, and 0 otherwise.

As it can be seen, for each new observation, all the N distances need to be computed. However, in the problem at hand, the feature vector has a low dimensionality, and the cardinality of the reference set is limited (as shown in Section III). Therefore, latency remains low, also in the case of limited computational capabilities as in our case.

III. EXPERIMENTAL VALIDATION

In this Section, the prototype developed for assessing the performances of the approach is presented at first. Thereafter, the selection of several parameters belonging to the processing algorithm is discussed. Finally, experimental results involving single or simultaneous multiple targets are presented in detail.

A. Measurement setup

As anticipated in the Introduction, a preliminary radar surveillance device prototype has been developed. Such a system is composed by two main components (Fig. 5):

- Infineon Distance2Go (D2G) board [55]. This FMCW radar board is endowed with an Infineon BGT24MTR11 transceiver, an Infineon XMC4200 32-bit ARM Cortex-M4 microcontroller, TX and RX antennas. These latter consist of two arrays, each one composed by eight rectangular patches (arranged in a 4×2 grid), resulting in a gain of 12 dBi, and horizontal and vertical half-power beamwidths of 42° and 20°, respectively.
- Raspberry Pi (RPi) 3 Model B+. This mini-PC communicates with the radar module by means of a COM port established through USB and it provides the power supply to the radar board with the same connection. The Raspberry can be powered by its own power supply or by a power bank.

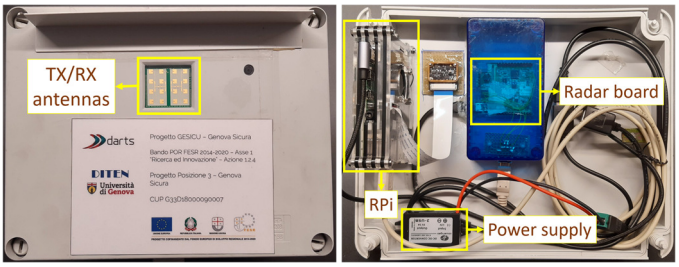

(a) (b)

Fig. 5. Radar surveillance device prototype. Frontal (a) and inner (b) view.

The parameters of the transmitted burst of chirps are reported in Table I, whereas Fig. 1 qualitatively shows some of them on a time-frequency representation. As can be seen from Table I, the CPI is slightly lower than $T_f/4$. This happens because the radar board has been set to operate with a duty-cycle close to 25%, keeping the board idle for 155.9 ms before the transmission of the next burst. This helps in lowering the power consumption and the temperature. With the adoption of the values listed in Table I, the radar characteristics reported in Table II are obtained (the Δr value is theoretical and it is usually worst in practice because of the windowing and non-idealities in the systems [67]). This table also reports the range accuracy of the adopted radar module and the noise figure of the transceiver, both provided by the technical documentation [55]. During the experimental campaigns, the maximum ranges at which pedestrians, motorcycles, cars, and trucks were detected are 13.5 m, 13.1 m, 23.8 m, and 23.9 m, respectively, thus, at least in the considered cases, the aliasing phenomenon has not been observed along the range dimension.

Assuming an expected maximum target radial speed of ± 30 km/h, a maximum displacement of about $\pm \Delta r/2$ can happen during the CPI; therefore, the target remains in the same range bin during this time interval and so range migration [29], [47] cannot occur. Because of the limited value of the maximum unambiguous radial velocity, the v_r-axis of the range-Doppler maps reported in the following cannot be used to directly estimate the radial velocity because of the aliasing phenomenon, as discussed in the previous Sections. Assuming again the previous expected maximum radial speed of a target, the range-Doppler coupling phenomenon [29] can cause an error on the estimated range up to $\pm 2\Delta r$. Regrettably, this error cannot be corrected a-posteriori, because of the Doppler aliasing inside the frame. In addition, the more advanced frequency modulations commonly used to delete this coupling [68], [69] are not available in the adopted low-cost radar module. However, it will be shown with the experimental results that a high accuracy in the classification of the targets can still be achieved.

TABLE I
FMCW PARAMETERS SET IN THE INFINEON DISTANCE2GO BOARD.

Parameter	Value	Parameter	Value
T_c	1.5 ms	N_c	21
B	200 MHz	T_{PRI}	2.1 ms
f_0	24.025 GHz	T_{CPI}	44.1 ms
N_s	64	T_f	200 ms

TABLE II
RADAR CHARACTERISTICS.

Parameter	Expression	Description	Value
Δr	$\frac{c}{2B}$	Range resolution	0.75 m
r_{max}	$\frac{N_s c}{4B}$	Maximum unambiguous range	24 m
a_1	-	Range accuracy up to 16 m ($\sigma = 1$ m^2)	± 30 cm
a_{10}	-	Range accuracy up to 24 m ($\sigma = 10$ m^2)	± 20 cm
$v_{r,max}$	$\frac{\lambda_0}{4T_{PRI}}$	Maximum unambiguous radial velocity	5.4 km/h
Δv_r	$\frac{\lambda_0}{2T_{CPI,eff}}$	Radial velocity resolution	0.5 km/h
η_f	-	Noise figure	12 dB

B. Parameter selection for window functions and IIR filter

In order to select proper values for K_{sf} and K_c, the passages of four different targets (a pedestrian, a motorcycle, a car, and a truck) in the experimental area have been recorded with the developed surveillance radar device. The collected data have been filtered and Fourier-transformed with K_c and K_{sf} varied in the intervals [0,0.9] and [0,5], respectively. Zero-padding with $N_R = 512$ and $N_D = 256$ is considered. The quality of the maps for each case is thus evaluated by means of the target-to-clutter ratio (TCR) [70] defined as follows

$$TCR(K_c, K_{sf}) = \frac{E_T\left[\left|M^{(K_c,K_{sf})}(q_{IF,n})\right|^2, n = 1, \dots N_f\right]}{E_C\left[\left|M^{(K_c,K_{sf})}(q_{IF,n})\right|^2, n = 1, \dots N_f\right]} \quad (22)$$

where $q_{IF,n}$ is the collection of samples for the nth frame, and N_f is the number of available frames. The operator $E_T(\cdot)$ computes the average on the regions of the input maps occupied by the target, whereas the operator $E_C(\cdot)$ acts on the remaining areas. Thereafter, the following performance index is computed

$$\widehat{TCR}(K_c, K_{sf}) = \frac{1}{4}\sum_{l} \widehat{TCR}_l(K_c, K_{sf}) \quad (23)$$

where $\widehat{TCR}_l$ is the function defined in (22) computed for one of the four recorded targets and normalized in [0,1]. The resulting $\widehat{TCR}$ is shown in Fig. 6; the higher value of this performance index happens for $K_c = 0.5$ and $K_{sf} = 3$, which will be used for the following tests.

It is interesting to highlight that the performance index obtained with this combination of parameters is 16.5% higher than the best achievable with the simpler and common single delay-line canceller (corresponding to $K_c = 0$). Moreover, this kind of filter does not need the selection of an updating period for the estimate of the clutter [50].

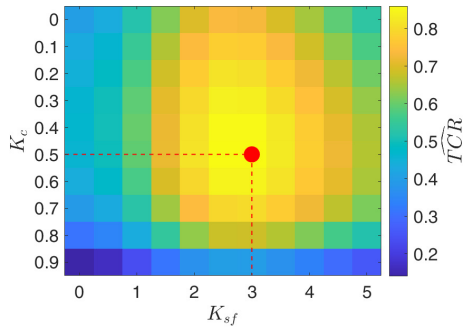

Fig. 6. Performance index $\widehat{TCR}$ for varying IIR parameter K_c and shape factor K_{sf}. The red dot indicates the position of the maximum value.

C. Hyperparameter selection for k-NN

Free hyperparameters of the k-NN method are the number of neighbors k and the metric adopted to measure the distance between points in the data space. These must be selected to provide a good generalization capability. To this end, the hyperparameters have been selected through a full grid search with 3-fold cross-validation evaluated on a dataset made of 182 observations. This latter has been built by recording several events involving single targets; this collection includes 88 cars, 31 pedestrians, 7 trucks, and 56 motorcycles. The target signatures on the range-Doppler maps are not clustered and tracked before computing the feature vectors, but they are simply thresholded with the parameter th_{RD}; this is done to make the learning process independent from the clustering and tracking parameters. The grid on which the optimal hyperparameters are searched is given by the cartesian product of the range [1,50] for the number of neighbors k and the set of metrics {Euclidean, Manhattan, Chebyshev}. The obtained optimal parameters are $k = 13$ and Euclidean distance. This

13-NN with Euclidean distance and reference dataset given by the 182 observations has been embedded in the processing chain of the developed surveillance radar prototype and used in the experimental trials reported in the following.

It is interesting to visualize the reference dataset to see how its points are spatially organized. Since the feature vectors have five components, a lower dimensional space for the visualization is adopted, given by the first three principal components c_1, c_2, and c_3 of the dataset [46], which explain nearly the 95% of the dataset variability. Fig. 7 shows the reference dataset projected on each couple of the three selected principal components. Clearly, except for pedestrians, the classes of points representing cars, trucks, and motorcycles appear severely overlapped. Therefore, it is difficult to expect a perfect separability of the classes.

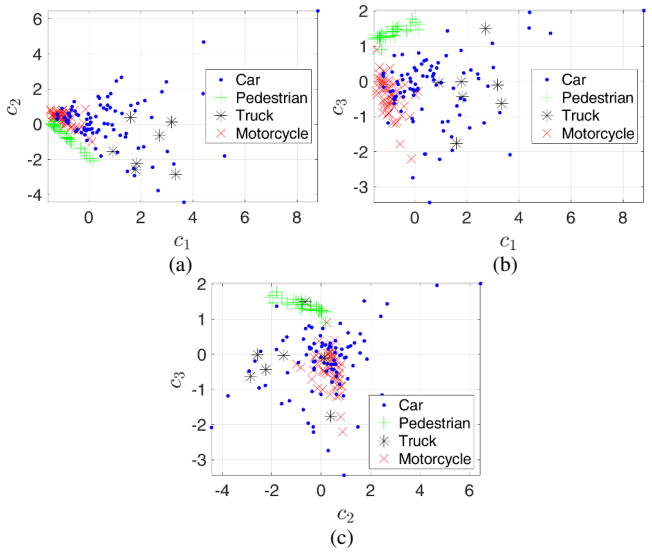

Fig. 7. Reference dataset projected on the (a) first and second, (b) first and third, (c) second and third principal components.

D. Experimental validation

This Section reports the results obtained by applying the proposed approach in two real operational scenarios. First, the capabilities of the system on situations involving single targets have been assessed. Finally, more challenging events involving the simultaneous presence of multiple targets will be evaluated.

Fig. 8 shows a picture of the monitored area used for the first experimental tests. As can be seen, there are several static metallic objects in the considered scenario, which are expected to generate sensible components of static clutter and multi-bounce reflections. It is worth noting that the radar is positioned in such a way that the road is contained in the main beam of the antenna. Consequently, the persistence of moving objects inside the footprints of the secondary lobes of the antennas is reduced (and contributions given by static objects are removed by the clutter and leakage removal block). Moreover, the tracking block should remove the related spurious and intermitting reflections. Nevertheless, this experimental setup can be considered quite challenging for radar applications. Table III reports the values of the parameters of the processing algorithm described in Section II. These have been empirically selected on the basis of preliminary tests (not reported for sake of brevity). In particular, the parameter th_{RD} has been initially set using radar frames acquired in absence of moving targets, to get the contributions of the background scene only spuriously returned by the IIR filter. The maximum amplitude for each frame is then computed and a first estimation of th_{RD} is obtained by averaging the maxima from the whole set of frames. However, the obtained value is often too low and can lead to an excessive number of points over threshold in the range-Doppler maps, which overload the following clustering and tracking block. Therefore, an empirical correction is applied to th_{RD} by observing a few examples of moving targets. It is worth noting that it has been chosen to not adopt a Constant False Alarm Rate (CFAR) methods to automatically determine this threshold since these algorithms may degrade the range resolution [53], which is already quite low in the adopted low-cost board, and the adopted simple thresholding strategy already allows to obtain good classification performances.

TABLE III
PARAMETERS VALUES SET IN THE PROCESSING ALGORITHM.

Parameter	Value	Parameter	Value
K_c	0.5	α	0.19
th_{RD}	2	R_{gate}	6
K_{sf}	3	N_u	7
ϵ	1.9	k	13
M	80	NN metric	Euclidean
th_v	0.25	N_R, N_D	512,256

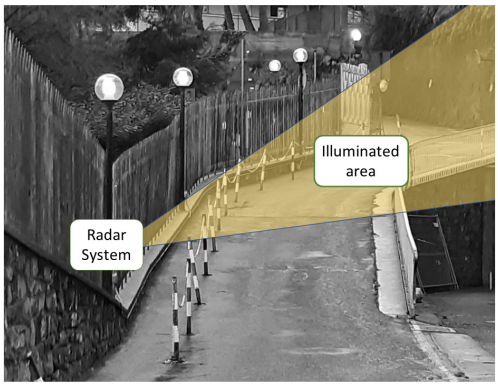

Fig. 8. View of the first monitored area used for the experimental validation.

1) Single targets

A test set of 20 single targets is considered here. It is made of 5 cars, 5 pedestrians, 5 motorcycles, and 5 trucks. Table IV reports the results in the form of a confusion matrix, showing a 90% overall accuracy in the recognition of the targets. Reducing the problem to a pedestrian/vehicle classification, and considering FMCW devices with recognition method tested in single-target scenarios only [32], [35], [37]–[39], [48], classification rates ranging from 75% to 97% were reported. Therefore, it can be concluded that the developed approach achieves a quite good accuracy, also considering that a higher-end hardware is often adopted in the cited works and that the capability to manage multiple targets simultaneously implies a performance trade-off.

The previous test has been repeated by removing one class from the k-NN reference dataset to study the behavior of the proposed approach when dealing with unknown targets. The test set is the same as before, thus allowing to simulate the presence of targets belonging to an unexpected class. Table V reports the confusion matrix obtained by removing the trucks from the reference set (the resulting optimal hyperparameters for the k-NN algorithm are $k = 4$ and the Euclidean distance). As expected, the unknown target is mislabeled. However, all trucks have been classified as cars, which can be considered the most similar class among the three remaining ones in the reference dataset.

TABLE IV
CONFUSION MATRIX FOR SINGLE TARGETS (PED = PEDESTRIAN, TRU = TRUCK, MOT = MOTORCYCLE).

Pred. \ *True*	**Car**	**Ped**	**Tru**	**Mot**
Car	4	0	0	0
Ped	0	5	0	1
Tru	1	0	5	0
Mot	0	0	0	4

TABLE V
CONFUSION MATRIX FOR SINGLE TARGETS (PED = PEDESTRIAN, TRU = TRUCK, MOT = MOTORCYCLE). TRUCKS REMOVED FROM THE REFERENCE SET.

Pred. \ *True*	**Car**	**Ped**	**Tru**	**Mot**
Car	5	0	5	0
Ped	0	5	0	1
Tru	0	0	0	0
Mot	0	0	0	4

2) Multiple targets

The collection of measurements for testing the capability of the system to manage a multi-target scenario includes 40 events, which involve a total of 45 pedestrians, 26 motorcycles, 20 cars, and 3 trucks. Table VI reports the resulting confusion matrix. The number of targets correctly classified is 73 on 94 total objects, resulting in an overall accuracy near to 80%. Such a result is comparable with those recently reported in [41] for automotive applications, where an accuracy of 85% has been achieved. However, it should be noted that in [41] different classes are considered, multiple high-end radars are employed, and bigger datasets have been adopted. It is important to note that the employed radar board is not able to provide azimuthal positions of the targets, since only a single receiving channel is available [16]. This can lead to situations in which two or more targets appear on the range-Doppler map as a single cloud of points (e.g., when two targets have the same radial velocity and range with respect to the radar, even if they are far away each other), and so there is no possibility for the method to distinguish between them. Almost all the missed targets are related to such cases. However, if these situations last only a limited number of frames, the tracking block can remedy it by storing different tracks for each real targets, thus allowing separated classifications, as shown in the following.

Finally, the higher error rate happens for the cars, especially when they are confused with motorcycles. This is probably due to the partial overlapping of the classes of points for cars and motorcycles in the reference dataset, as already previously reported in Fig. 7. In the following sub-sections, a deeper insight on the behavior of the proposed algorithm for three meaningful multi-target events is provided.

As done for the single-target case, the output of the system has been analyzed also after the removal of the trucks from the reference set, and the related confusion matrix is reported in Table VII. As can be seen, except for the truck class, the performance is quite similar to the previous case, whereas two of the three trucks are recognized as cars.

TABLE VI
CONFUSION MATRIX FOR MULTI-TARGET EVENTS (PED = PEDESTRIAN, TRU = TRUCK, MOT = MOTORCYCLE).

Pred. \ *True*	**Car**	**Ped**	**Tru**	**Mot**
Car	11	0	0	0
Ped	0	35	0	1
Tru	2	0	3	0
Mot	6	3	0	24
missed	1	7	0	1

TABLE VII
CONFUSION MATRIX FOR MULTI-TARGET EVENTS (PED = PEDESTRIAN, TRU = TRUCK, MOT = MOTORCYCLE). TRUCKS REMOVED FROM THE REFERENCE SET.

Pred. \ *True*	**Car**	**Ped**	**Tru**	**Mot**
Car	12	0	2	1
Ped	0	35	1	0
Tru	0	0	0	0
Mot	7	3	0	24
missed	1	7	0	1

a) Test 1

This first test event involves two pedestrians and a car. Initially, only a single pedestrian appears in the scene, and it is moving toward the radar, but in a short time a second pedestrian enters the scene moving away from the device. After that, the pedestrians intersect and the approaching pedestrian exits the radar beam, and a departing car also appears. The output of the processing chain up to the tracking block is illustrated in Fig. 9(a)-(f), where the identified clusters are shown on the range-Doppler maps with different colors to distinguish between the corresponding tracks. In the same figures the identification number of each track is reported, too. The approaching pedestrian (ID 1) is shown in Fig. 9(a). When also the departing pedestrian appears in the radar beam, they are indistinct on the range-Doppler map, as can be seen in Fig. 9(b), but as soon as they get a sufficient separation along the range and Doppler dimensions, the algorithm assigns a distinct cluster and track (ID 3) to the second pedestrian (Fig. 9(c)). After that the approaching pedestrian (ID 1) leaves the scene, the car enters it, but, because the several reflections generated by its metallic structures spread over the map, initially it is not distinguished from the pedestrian cluster (Fig. 9(d)). However, after 5 frames (corresponding to 1 s), the clusters belonging to the two targets are separated and a proper track (ID 5) is assigned to the car (Fig. 9(e)). Finally, Fig. 9(f) shows the departing pedestrian (ID 3) and car (ID 5) moving away. Therefore, the algorithm has been able to coherently follow the real targets that appeared in

the scene, also correctly solving the situations in which the targets were not immediately distinguishable on the map.

For completeness, the estimated range and radial velocity of each cluster (considered as a point target) in the reported frames are superimposed on the images in Fig. 9. In particular, the estimated range $\tilde{r}$ is directly obtained from the state vector (see Section II.D), whereas the radial velocity $\tilde{v}_r$ is estimated by considering the displacement between two consecutive frames (when a new track born, it has no previous estimated range, thus its radial velocity is indicated as "Not Available"). Indeed, the radial velocity information available from the range-Doppler maps are affected by ambiguity, and thus may be different from the actual ones. Moreover, the state variables related to the velocity in the tracking method are defined on the wrapped range-Doppler maps and therefore they do not directly provide the radial velocity. It is also worth remarking that a high range and velocity accuracy is not needed, since the purpose of the tracking block is to just maintain the association between the cluster tags on the range-Doppler maps and the targets.

The output of the classifier block is reported in Table VIII. The same table reports the estimated average radial velocities (derived from the tracking results) and the direction of each target (identified with the same numbers adopted in the legends of Fig. 9). All the target types are correctly predicted, and the average radial speeds and directions are compatible with the observed targets.

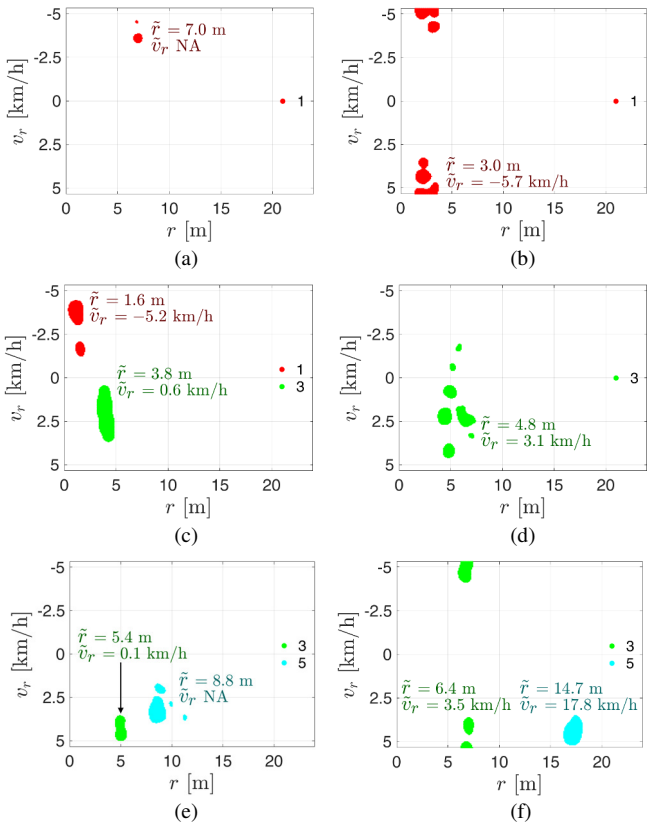

Fig. 9. Tracked clusters on range-Doppler maps in temporal order. (a) Approaching pedestrian (ID 1), (b) indistinct pedestrians, (c) pedestrians (ID 1 and 3) after intersecting, (d) indistinct pedestrian and car, (e) pedestrian (ID 3) and car (ID 5) after intersecting, and (f) departing pedestrian (ID 3) and car (ID 5). The legend shows the identification number of each track. The estimated ranges and radial velocities of the centroids are superimposed on the images.

TABLE VIII
TRUE AND PREDICTED CLASSES FOR EACH TRACKED TARGET, ALONG WITH ESTIMATED AVERAGE RADIAL SPEED AND DIRECTION.

n. ID	True class	Predicted class	Av. radial speed	Direction
1	Pedestrian	Pedestrian	-3.6 km/h	Approaching
3	Pedestrian	Pedestrian	2.3 km/h	Departing
5	Car	Car	17.5 km/h	Departing

b) Test 2

A pedestrian and a truck are present in the second test case. Both targets move toward the device and the truck is the first to exit the illuminated scene. Initially, only the truck (ID 1) is detected (Fig. 10(a)), because the pedestrian, that has generally the lowest RCS among the considered types of targets, is still quite far. When the pedestrian reaches a range of about 10 m, it is detected, and a track (ID 2) is assigned to it (Fig. 10(b)). Fig. 10(b) and Fig. 10(c) show that the large metallic body of a truck usually exhibits several reflection points that spread on the range-Doppler map. Once the truck exits the illuminated scene, only the approaching pedestrian (ID 2) is followed (Fig. 10(d)).

Table IX reports the results of the classification, along with the estimated average radial velocities and the directions of each track. Again, the target types, the average radial speeds, and the directions are correctly estimated.

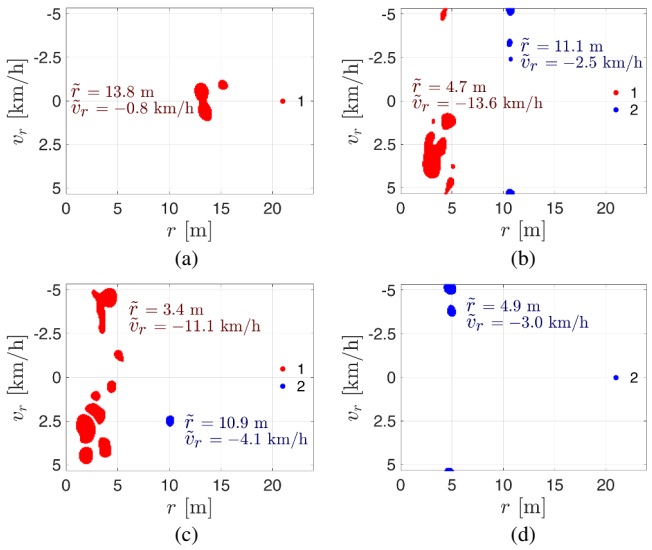

Fig. 10. Tracked clusters on range-Doppler maps in temporal order. (a) Approaching truck (ID 1), (b), (c) separated pedestrian (ID 2) and truck (ID 1), and (d) approaching pedestrian (ID 2). The legend shows the identification number of each track. The estimated ranges and radial velocities of the centroids are superimposed on the images.

TABLE IX
TRUE AND PREDICTED CLASSES FOR EACH TRACKED TARGET, ALONG WITH ESTIMATED AVERAGE RADIAL SPEED AND DIRECTION.

n. ID	True class	Predicted class	Av. radial speed	Direction
1	Truck	Truck	-7.1 km/h	Approaching
2	Pedestrian	Pedestrian	-2.8 km/h	Approaching

c) Test 3

A pedestrian and a motorcycle are involved in the third test event. The two targets move in opposite directions, with the pedestrian, which is the first to enters the radar beam, walking toward the radar and the motorcycle that is departing at a quite high speed. Fig. 11(a) shows the approaching pedestrian (ID 1). When the motorcycle enters the monitored zone, it is located in an area of the range-Doppler map that does not allow to distinguish the two clouds of points (Fig. 11(b)), but after only two frames the two targets get a sufficient separation to be correctly clustered and tracked (Fig. 11(c)). Near the end of the event, Fig. 11(d) illustrates the approaching pedestrian (ID 1) and the departing motorcycle (ID 2) moving away from each other. Again, the processing has been able to correctly solve a situation in which the two targets were not immediately distinguishable on the map. Table X reports the correct recognition of the target types and of their movements. Concerning computational times, the processing of the 20 frames recorded for the current event required about 0.9 s on the Raspberry Pi 3B+ embedded PC used in the prototype.

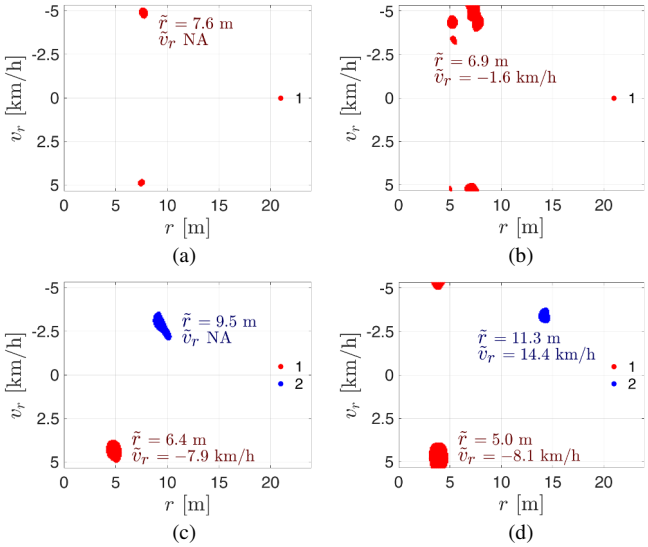

Fig. 11. Tracked clusters on range-Doppler maps in temporal order. (a) Approaching pedestrian (ID 1), (b) indistinct pedestrian and motorcycle, (c) after intersection of pedestrian (ID 1) and motorcycle (ID 2), and (d) approaching pedestrian (ID 1) and departing motorcycle (ID 2). The legend shows the identification number of each track. The estimated ranges and radial velocities of the centroids are superimposed on the images.

TABLE X
TRUE AND PREDICTED CLASS FOR EACH TRACKED TARGET, ALONG WITH ESTIMATED AVERAGE RADIAL SPEED AND DIRECTION.

n. ID	True class	Predicted class	Av. radial speed	Direction
1	Pedestrian	Pedestrian	-7.6 km/h	Approaching
2	Motorcycle	Motorcycle	27.4 km/h	Departing

3) Validation in a different scenario

In order to assess the capabilities of the developed approach to be reused in a different scenario, a second monitored area has been considered. In this new case, the radar is positioned on the side of a different road. Moreover, the radar looks down the road from a higher position than in the previous situation. Consequently, side obstacles and clutter are different. The relative positions between the targets and the radar are also different from the previous scenario. The reference dataset used for the k-NN is the same employed in the previous Sections. Moreover, the values of the parameters reported in Table III have not been changed.

To provide a further insight on the performance of the developed radar setup, the probabilities of detection of a target before the tracking block (i.e., using the output of DBSCAN for each frame) have been computed considering all the available measured frames, and resulted equal to 70% (pedestrians), 84% (motorcycles), 88% (cars), and 92% (trucks). It is interesting to note that such quantities grow with the increase of the magnitudes of the RCS for the considered classes, as expected since a stronger signal is on average received. It is however worth remarking that at this point classification is not yet performed, and the subsequent tracking and classification blocks can affect the final detection probabilities.

To test the classification capabilities, a test set of 28 single targets (7 cars, 7 pedestrians, 7 motorcycles, and 7 trucks) is considered for the single-target case. Table XI reports the resulting confusion matrix, showing an overall accuracy near to 80%. For the multi-target case, 46 events have been processed, involving a total of 57 pedestrians, 14 motorcycles, 22 cars, and 9 trucks. The confusion matrix reported in Table XII shows an overall accuracy of 73% approximately. As can be seen, the proposed technique presents good generalization capabilities, which allows reusing the calibration data at least when the considered scenarios have an overall similar structure. However, it is expected that a recalibration would be required if the radar positioning or the type of scenario became significantly different than those used in the calibration.

TABLE XI
CONFUSION MATRIX FOR SINGLE TARGETS (PED = PEDESTRIAN, TRU = TRUCK, MOT = MOTORCYCLE). SECOND SCENARIO.

		True			
		Car	**Ped**	**Tru**	**Mot**
Pred.	**Car**	5	0	2	0
	Ped	0	6	0	0
	Tru	1	0	4	0
	Mot	1	1	1	7

TABLE XII
CONFUSION MATRIX FOR MULTI-TARGET EVENTS (PED = PEDESTRIAN, TRU = TRUCK, MOT = MOTORCYCLE). SECOND SCENARIO.

		True			
		Car	**Ped**	**Tru**	**Mot**
Pred.	**Car**	18	0	2	0
	Ped	0	38	0	0
	Tru	1	0	6	0
	Mot	2	9	1	12
	Missed	1	10	0	2

IV. CONCLUSIONS

In the present paper, a novel short-range surveillance technique based on low-cost FMCW radar technology has been presented. The data processing method is based on an ad-hoc chain composed by several blocks, which perform clutter and leakage removal by means of an IIR filter (endowed with step initialization), clustering with the DBSCAN algorithm applied

on wrapped range-Doppler maps, tracking of clusters with a Benedict-Bordner α-β filter, features extraction, and finally classification by means of a k-NN classifier. A prototype of the system, equipped with a low-cost Distance2Go radar module from Infineon and a Raspberry Pi 3 Model B+ mini-PC, has been assembled and used to experimentally test the developed procedure in real operating environments. The obtained results show that the developed technique, although relying on data provided by low-cost components with limited radar resolutions and computational capabilities, can effectively recognize the targets, even in complex situations involving multiple simultaneous objects with different velocities and moving directions. Moreover, the system can be reused in different scenarios without the need of performing again a calibration of the method parameters, provided that the new configuration is not too different from the one used to create the reference dataset. Further developments will be aimed at including more advanced processing blocks, e.g., tracking schemes based on probabilistic models of associations. Moreover, the integration of enhanced radar boards, e.g., able to provide the azimuthal positions of the targets through directions of arrival estimations or working at higher frequencies, will be also pursued to increase the classification capabilities especially in the presence of multiple targets with small distances.

ACKNOWLEDGMENT

The authors would like to thank Alessandro Delucchi and Roberto Vio (Darts Engineering Srl, Genoa, Italy) for their kind support during the development phase and the experimental activities presented in this article.

REFERENCES

[1] P. Withington, H. Fluhler, and S. Nag, "Enhancing homeland security with advanced UWB sensors," *IEEE Microw. Mag.*, vol. 4, no. 3, pp. 51–58, Sep. 2003.

[2] F. Colone, D. Pastina, P. Falcone, and P. Lombardo, "WiFi-based passive ISAR for high-resolution cross-range profiling of moving targets," *IEEE Trans. Geosci. Remote Sens.*, vol. 52, no. 6, pp. 3486–3501, Jun. 2014.

[3] G. Gennarelli, G. Vivone, P. Braca, F. Soldovieri, and M. G. Amin, "Multiple extended target tracking for through-wall radars," *IEEE Trans. Geosci. Remote Sens.*, vol. 53, no. 12, pp. 6482–6494, 2015.

[4] A. Randazzo, C. Ponti, A. Fedeli, C. Estatico, P. D'Atanasio, M. Pastorino, *et al.*, "A two-step inverse-scattering technique in variable-exponent Lebesgue spaces for through-the-wall microwave imaging: Experimental results," *IEEE Trans. Geosci. Remote Sens.*, vol. 59, no. 9, pp. 7189–7200, Sep. 2021.

[5] G. Gennarelli, I. Catapano, X. Dérobert, and F. Soldovieri, "A ground penetrating radar imaging approach for a heterogeneous subsoil with a vertical permittivity gradient," *IEEE Trans. Geosci. Remote Sens.*, 2020.

[6] A. Benedetto and L. Pajewski, *Civil Engineering Applications of Ground Penetrating Radar*. Cham, Switzerland: Springer, 2015.

[7] S. Lambot and F. André, "Full-wave modeling of near-field radar data for planar layered media reconstruction," *IEEE Trans. Geosci. Remote Sens.*, vol. 52, no. 5, pp. 2295–2303, May 2014.

[8] M. Pastorino, A. Randazzo, A. Fedeli, A. Salvadè, S. Poretti, M. Maffongelli, *et al.*, "A microwave tomographic system for wood characterization in the forest products industry," *Wood Mater. Sci. Eng.*, vol. 10, no. 1, pp. 75–85, 2015.

[9] T. Negishi, G. Gennarelli, F. Soldovieri, Y. Liu, and D. Erricolo, "Radio frequency tomography for nondestructive testing of pillars," *IEEE Trans. Geosci. Remote Sens.*, vol. 58, no. 6, pp. 3916–3926, Jun. 2020.

[10] J. M. Munoz-Ferreras, F. Perez-Martinez, J. Calvo-Gallego, A. Asensio-Lopez, B. P. Dorta-Naranjo, and A. Blanco-del-Campo, "Traffic surveillance system based on a high-resolution radar," *IEEE Trans. Geosci. Remote Sens.*, vol. 46, no. 6, pp. 1624–1633, Jun. 2008.

[11] S. Saponara, M. S. Greco, and F. Gini, "Radar-on-chip/in-package in autonomous driving vehicles and intelligent transport systems: opportunities and challenges," *IEEE Signal Process. Mag.*, vol. 36, no. 5, pp. 71–84, Sep. 2019.

[12] S. Fontul, A. Paixão, M. Solla, and L. Pajewski, "Railway track condition assessment at network level by frequency domain analysis of GPR data," *Remote Sens.*, vol. 10, no. 4, 2018.

[13] G. L. Charvat, *Small and Short-Range Radar Systems*. Boca Raton: CRC Press, Taylor & Francis Group, 2014.

[14] C. Li, Z. Peng, T.-Y. Huang, T. Fan, F.-K. Wang, T.-S. Horng, *et al.*, "A review on recent progress of portable short-range noncontact microwave radar systems," *IEEE Trans. Microw. Theory Tech.*, vol. 65, no. 5, pp. 1692–1706, May 2017.

[15] Pao-Jen Wang, Chi-Min Li, Cheng-Ying Wu, and Hsueh-Jyh Li, "A channel awareness vehicle detector," *IEEE Trans. Intell. Transp. Syst.*, vol. 11, no. 2, pp. 339–347, Jun. 2010.

[16] S. Saponara and B. Neri, "Radar sensor signal acquisition and multidimensional FFT processing for surveillance applications in transport systems," *IEEE Trans. Instrum. Meas.*, vol. 66, no. 4, pp. 604–615, Apr. 2017.

[17] A. Mukhtar, L. Xia, and T. B. Tang, "Vehicle detection techniques for collision avoidance systems: A review," *IEEE Trans. Intell. Transp. Syst.*, vol. 16, no. 5, pp. 2318–2338, Oct. 2015.

[18] D.-H. Jung, H.-S. Kang, C.-K. Kim, J. Park, and S.-O. Park, "Sparse scene recovery for high-resolution automobile FMCW SAR via scaled compressed sensing," *IEEE Trans. Geosci. Remote Sens.*, vol. 57, no. 12, pp. 10136–10146, Dec. 2019.

[19] C. Ding, H. Hong, Y. Zou, H. Chu, X. Zhu, F. Fioranelli, *et al.*, "Continuous human motion recognition with a dynamic range-Doppler trajectory method based on FMCW radar," *IEEE Trans. Geosci. Remote Sens.*, vol. 57, no. 9, pp. 6821–6831, Sep. 2019.

[20] Y. Nan, X. Huang, and Y. J. Guo, "A millimeter-wave GCW-SAR based on deramp-on-receive and piecewise constant Doppler imaging," *IEEE Trans. Geosci. Remote Sens.*, vol. 58, no. 1, pp. 680–690, Jan. 2020.

[21] C. Q. Mayoral, C. Garcia Gonzalez, J. C. I. Galarregui, D. Marin, D. Gaston, C. Miranda, *et al.*, "Water content continuous monitoring of grapevine xylem tissue using a portable low-power cost-effective FMCW radar," *IEEE Trans. Geosci. Remote Sens.*, vol. 57, no. 8, pp. 5595–5605, Aug. 2019.

[22] B. Vandersmissen, N. Knudde, A. Jalalvand, I. Couckuyt, A. Bourdoux, W. De Neve, *et al.*, "Indoor person identification using a low-power FMCW radar," *IEEE Trans. Geosci. Remote Sens.*, vol. 56, no. 7, pp. 3941–3952, Jul. 2018.

[23] B. Yektakhah and K. Sarabandi, "All-directions through-the-wall imaging using a small number of moving omnidirectional bi-static FMCW transceivers," *IEEE Trans. Geosci. Remote Sens.*, vol. 57, no. 5, pp. 2618–2627, May 2019.

[24] A. Ganis, E. M. Navarro, B. Schoenlinner, U. Prechtel, A. Meusling, C. Heller, *et al.*, "A portable 3-D imaging FMCW MIMO radar demonstrator with a 24x24 antenna array for medium-range applications," *IEEE Trans. Geosci. Remote Sens.*, vol. 56, no. 1, pp. 298–312, Jan. 2018.

[25] D. Jasteh, E. G. Hoare, M. Cherniakov, and M. Gashinova, "Experimental low-terahertz radar image analysis for automotive terrain sensing," *IEEE Geosci. Remote Sens. Lett.*, vol. 13, no. 4, pp. 490–494, Apr. 2016.

[26] F. Fioranelli, S. Salous, and X. Raimundo, "Frequency-modulated interrupted continuous wave as wall removal technique in through-the-wall imaging," *IEEE Trans. Geosci. Remote Sens.*, vol. 52, no. 10, pp. 6272–6283, Oct. 2014.

[27] A. Anghel, G. Vasile, R. Cacoveanu, C. Ioana, and S. Ciochina, "Short-range wideband FMCW radar for millimetric displacement measurements," *IEEE Trans. Geosci. Remote Sens.*, vol. 52, no. 9, pp. 5633–5642, Sep. 2014.

[28] R. Wang, Yun-Hua Luo, Yun-Kai Deng, Zhi-Ming Zhang, and Yue Liu, "Motion compensation for high-resolution automobile FMCW SAR," *IEEE Geosci. Remote Sens. Lett.*, vol. 10, no. 5, pp. 1157–1161, Sep. 2013.

[29] M. A. Richards, *Fundamentals of Radar Signal Processing*. New York, NY: McGraw-Hill, 2014.

[30] A. Asensio Lopez, A. Duque de Quevedo, F. Salmeron Yuste, J. Munoz Dekamp, V. Aparicio Mequiades, V. Medel Cortes, *et al.*, "Coherent

signal processing for traffic flow measuring radar sensor," *IEEE Sens. J.*, vol. 18, no. 12, pp. 4803–4813, Jun. 2018.
[31] Y. Zhao and Y. Su, "Vehicles detection in complex urban scenes using gaussian mixture model with FMCW radar," *IEEE Sens. J.*, vol. 17, no. 18, pp. 5948–5953, Sep. 2017.
[32] Y. Lee, H. Choo, S. Kim, and H. Kim, "RCS based target recognition with real FMCW radar implementation," *Microw. Opt. Technol. Lett.*, vol. 58, no. 7, pp. 1745–1750, Jul. 2016.
[33] H.-T. Chou, H.-K. Ho, and T.-P. Chang, "Effectiveness of moving signal-average method in K band FMCW radar for short-range vehicle detection using antennas with narrow beam widths," *Radio Sci.*, vol. 53, no. 3, pp. 344–356, Mar. 2018.
[34] H.-J. Cho and M.-T. Tseng, "A support vector machine approach to CMOS-based radar signal processing for vehicle classification and speed estimation," *Math. Comput. Model.*, vol. 58, no. 1–2, pp. 438–448, Jul. 2013.
[35] R. Perez, F. Schubert, R. Rasshofer, and E. Biebl, "Single-frame vulnerable road users classification with a 77 GHz FMCW radar sensor and a convolutional neural network," in *Proc. 19th Int. Radar Symp.*, Bonn, Germany, 2018, pp. 1–10.
[36] A. Mazzinghi, L. Facheris, F. Cuccoli, and A. Freni, "2.5D physical optics based algorithm for vehicles classification through a FM-CW radar," in *Proc. 15th Eur. Radar Conf.*, Madrid, Spain, 2018, pp. 257–260.
[37] T. Gao, Z. Lai, Z. Mei, and Q. Wu, "Hybrid SVM-CNN classification technique for moving targets in automotive FMCW radar system," in *Proc. 11th Int. Conf. Wirel. Commun. Signal Process.*, Xi'an, China, 2019, pp. 1–6.
[38] S. Heuel and H. Rohling, "Pedestrian recognition based on 24 GHz radar sensors," in *Ultra-Wideband Radio Technologies for Communications, Localization and Sensor Applications*, R. Thom, Ed. InTech, 2013.
[39] S. Lee, Y.-J. Yoon, J.-E. Lee, and S.-C. Kim, "Human–vehicle classification using feature-based SVM in 77-GHz automotive FMCW radar," *IET Radar Sonar Navig.*, vol. 11, no. 10, pp. 1589–1596, Oct. 2017.
[40] R. Prophet, M. Hoffmann, M. Vossiek, C. Sturm, A. Ossowska, W. Malik, *et al.*, "Pedestrian classification with a 79 GHz automotive radar sensor," in *Proc. 19th Int. Radar Symp.*, Bonn, Germany, 2018, pp. 1–6.
[41] O. Schumann, J. Lombacher, M. Hahn, C. Wohler, and J. Dickmann, "Scene understanding with automotive radar," *IEEE Trans. Intell. Veh.*, vol. 5, no. 2, pp. 188–203, 2020.
[42] S.-L. Jeng, W.-H. Chieng, and H.-P. Lu, "Estimating speed using a side-looking single-radar vehicle detector," *IEEE Trans. Intell. Transp. Syst.*, vol. 15, no. 2, pp. 607–614, Apr. 2014.
[43] D. Felguera-Martin, J.-T. Gonzalez-Partida, P. Almorox-Gonzalez, and M. Burgos-García, "Vehicular traffic surveillance and road lane detection using radar interferometry," *IEEE Trans. Veh. Technol.*, vol. 61, no. 3, pp. 959–970, Mar. 2012.
[44] A. Angelov, A. Robertson, R. Murray-Smith, and F. Fioranelli, "Practical classification of different moving targets using automotive radar and deep neural networks," *IET Radar Sonar Navig.*, vol. 12, no. 10, pp. 1082–1089, Oct. 2018.
[45] I. Urazghildiiev, R. Ragnarsson, P. Ridderstrom, A. Rydberg, E. Ojefors, K. Wallin, *et al.*, "Vehicle classification based on the radar measurement of height profiles," *IEEE Trans. Intell. Transp. Syst.*, vol. 8, no. 2, pp. 245–253, Jun. 2007.
[46] C. M. Bishop, *Pattern Recognition and Machine Learning*. New York: Springer, 2006.
[47] C. Özdemir, *Inverse Synthetic Aperture Radar Imaging with MATLAB Algorithms*. Hoboken, NJ: Wiley, 2012.
[48] L. Du, L. Li, B. Wang, and J. Xiao, "Micro-Doppler feature extraction based on time-frequency spectrogram for ground moving targets classification with low-resolution radar," *IEEE Sens. J.*, vol. 16, no. 10, pp. 3756–3763, May 2016.
[49] R. H. Fletcher and D. W. Burlage, "Improved moving-target-indicator filtering for phased array radars," Adv. Sens. Directorate, U.S. Army Missile Res., Develop. Eng. Lab., U.S. Army Missile Command, Redstone Arsenal, Huntsville, AL, USA, Tech. Rep. RE-73-17, 1973.
[50] M. Ash, M. Ritchie, and K. Chetty, "On the application of digital moving target indication techniques to short-range FMCW radar data," *IEEE Sens. J.*, vol. 18, no. 10, pp. 4167–4175, May 2018.
[51] M. Ester, H.-P. Kriegel, J. Sander, and X. Xu, "A density-based algorithm for discovering clusters in large spatial databases with noise," in *Proc. Second Int. Conf. Knowl. Discov. Data Min.*, Portland, Oregon, 1996, pp. 226–231.
[52] B. R. Mahafza and A. Z. Elsherbeni, *MATLAB Simulations for Radar Systems Design*. Boca Raton, FL: CRC Press/Chapman & Hall, 2004.
[53] M. I. Skolnik, *Introduction to Radar Systems*. McGraw-Hill, 2001.
[54] K. V. Mardia and P. E. Jupp, *Directional Statistics*. Chichester; New York: J. Wiley, 2010.
[55] Infineon Technologies AG, "AN543 - Distance2Go – XENSIV™ 24 GHz radar demo kit with BGT24MTR11 and XMC4200 32-bit ARM® Cortex™-M4 MCU for ranging, movement and presence detection (board version V1.1)." .
[56] W. Shi and S. Dustdar, "The promise of edge computing," *Computer*, vol. 49, no. 5, pp. 78–81, May 2016.
[57] E. Giusti and M. Martorella, "Range doppler and image autofocusing for FMCW inverse synthetic aperture radar," *IEEE Trans. Aerosp. Electron. Syst.*, vol. 47, no. 4, pp. 2807–2823, 2011.
[58] M. Jankiraman, *FMCW radar design*. Norwood, Massachusetts: Artech House, 2018.
[59] D. Simon and Tien Li Chia, "Kalman filtering with state equality constraints," *IEEE Trans. Aerosp. Electron. Syst.*, vol. 38, no. 1, pp. 128–136, Jan. 2002.
[60] Y. Bar-Shalom, X.-R. Li, and T. Kirubarajan, *Estimation with Applications to Tracking and Navigation*. New York, USA: John Wiley & Sons, Inc., 2001.
[61] M. A. Richards, J. Scheer, W. A. Holm, and W. L. Melvin, Eds., *Principles of modern radar*. Raleigh, NC: SciTech Pub, 2010.
[62] European Commission. Joint Research Centre. Institute for the Protection and the Security of the Citizen., *Radar cross section measurements of pedestrian dummies and humans in the 24/77 GHz frequency bands: establishment of a reference library of RCS signatures of pedestrian dummies in the automotive radar bands.* LU: Publications Office, 2013.
[63] E. Schubert, M. Kunert, W. Menzel, J. Fortuny-Guasch, and J.-M. Chareau, "Human RCS measurements and dummy requirements for the assessment of radar based active pedestrian safety systems," in *2013 14th Int. Radar Symp. IRS*, 2013, vol. 2, pp. 752–757.
[64] I. Bilik, J. Tabrikian, and A. Cohen, "GMM-based target classification for ground surveillance Doppler radar," *IEEE Trans. Aerosp. Electron. Syst.*, vol. 42, no. 1, pp. 267–278, Jan. 2006.
[65] A. Eryildirim and I. Onaran, "Pulse Doppler radar target recognition using a two-stage SVM procedure," *IEEE Trans. Aerosp. Electron. Syst.*, vol. 47, no. 2, pp. 1450–1457, Apr. 2011.
[66] M. Jahangir, K. M. Ponting, and J. W. O'Loghlen, "Robust Doppler classification technique based on hidden Markov models," *IEE Proc. - Radar Sonar Navig.*, vol. 150, no. 1, p. 33, 2003.
[67] J. Scheer and J. L. Kurtz, Eds., *Coherent Radar Performance Estimation*. Boston: Artech House, 1993.
[68] S. Saponara, M. Greco, E. Ragonese, G. Palmisano, and B. Neri, *Highly Integrated Low-Power Radars*. Boston: Artech House, 2014.
[69] V. Issakov, *Microwave Circuits for 24 GHz Automotive Radar in Silicon-Based Technologies*. Heidelberg ; New York: Springer, 2010.
[70] F. H. C. Tivive, A. Bouzerdoum, and M. G. Amin, "A subspace projection approach for wall clutter mitigation in through-the-wall radar imaging," *IEEE Trans. Geosci. Remote Sens.*, vol. 53, no. 4, pp. 2108–2122, Apr. 2015.

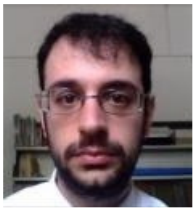

Emanuele Tavanti (Member, IEEE) received the Laurea degree in electronic engineering and the Ph.D. degree in science and technology for electronic and telecommunications engineering, from the University of Genoa, Genoa, Italy, in 2015 and 2019, respectively. He is currently a Research Fellow with the Department of Electrical, Electronic, Telecommunications Engineering, and Naval Architecture of the University of Genoa. His research activity is focused on computational methods for direct and inverse electromagnetic scattering, biomedical applications of bioimpedance measurement technologies, security applications of radar technologies, and atmospheric propagation.

Ali Rizik (Student Member, IEEE) received the B.S. degree in electronic and the M.Sc. degree in signal, telecom, image, and speech processing, from the Faculty of Science, Lebanese University, in 2014 and 2016, respectively. He is currently pursuing the Ph.D. degree in science and technology for electronic and telecommunication engineering with the Department of Naval, Electrical, Electronic, and Telecommunications Engineering (DITEN), University of Genoa. From April to August 2016, he was an Internship with ULCO University, France. His main research interest includes machine learning applications, radar signal processing, and radar target classification for security applications.

Alessandro Fedeli (Member, IEEE) received the B.Sc. and M.Sc. degrees in electronic engineering and the Ph.D. degree in science and technology for electronic and telecommunications engineering from the University of Genoa, Genoa, Italy, in 2011, 2013, and 2017, respectively. He is currently an Assistant Professor with the Department of Electrical, Electronic, Telecommunications Engineering, and Naval Architecture, University of Genoa. His research activities, carried out at the Applied Electromagnetics Laboratory, are mainly focused on the development and the application of computational methods for the solution of forward and inverse scattering problems, and electromagnetic imaging. He has coauthored more than 130 scientific contributions published in international journals, conference proceedings, and book chapters. Dr. Fedeli is member of the IEEE Antennas and Propagation Society, the Italian Society of Electromagnetism, and the Interuniversity Center for the Interaction between Electromagnetic Fields and Biosystems.

Daniele D. Caviglia (Life Member, IEEE) graduated in electronic engineering and specialized in computer engineering from the University of Genoa, Genoa, Italy, in 1980 and 1982, respectively. In 1983, he joined the Institute of Electrical Engineering, University of Genoa, as Assistant Professor of Electronics. Since 1984, he has been with the Department of Biophysical and Electronic Engineering (DIBE), as Associate Professor from 1992 and as Full Professor from 2000. From 2002 to 2008, he was the Director of DIBE. He is currently with the Department of Electrical, Electronics and Telecommunications Engineering and Naval Architecture (DITEN), University of Genoa, teaching courses in electronic systems for telecommunications, electronic devices and circuits, and microelectronics. He is also active in the development of innovative solutions for environmental monitoring for civil protection and security applications. His research interests include the design of electronic circuits and systems for telecommunications, electronic equipment for health and safety, and energy harvesting techniques for Internet of Things (IoT) applications.

Andrea Randazzo (Senior Member, IEEE) received the laurea degree in telecommunication engineering and the Ph.D. degree in information and communication technologies from the University of Genoa, Genoa, Italy, in 2001 and 2006, respectively. He is currently a Full Professor of electromagnetic fields at the Department of Electrical, Electronic, Telecommunication Engineering, and Naval Architecture, University of Genoa. He has coauthored the book Microwave Imaging Methods and Applications (Artech House, 2018) and more than 280 articles published in journals and conference proceedings. His primary research interests are in the field of microwave imaging, inverse-scattering techniques, radar processing, numerical methods for electromagnetic scattering and propagation, electrical tomography, and smart antennas.